



Copyright Notice

This paper was published in *Optics Express* and is made available as an electronic reprint with the permission of OSA. The paper can be found at the following URL on the OSA website: <http://dx.doi.org/10.1364/OE.20.010816>. Systematic or multiple reproduction or distribution to multiple locations via electronic or other means is prohibited and is subject to penalties under law.

(Article begins on next page)

Simulating light scattering from supported plasmonic nanowires

Vladimir D. Miljković,^{1,*} Timur Shegai,¹ Peter Johansson,^{1,2} and Mikael Käll¹

¹Department of Applied Physics, Chalmers University of Technology, 412 96 Göteborg, Sweden

²School of Science and Technology, Örebro University, 701 82 Örebro, Sweden

*vladimir.miljkovic@chalmers.se

Abstract: We present a method for calculating the differential scattering cross sections from nanostructures close to an interface separating two semi-infinite dielectric media. The method combines a fast finite element software (Comsol multiphysics), used for calculations of the fields around and inside the structure, and the Green's functions method, which is used to find the far field distribution from the calculated total fields inside the nanostructure. We apply the method to calculations of scattering spectra from silver nanowires supported by an air-glass interface, a system that is of high current interest in relation to various nanophotonics applications. The results are analyzed in relation to analytical models and compared to experimentally measured spectra, to which we find a good agreement.

©2012 Optical Society of America

OCIS codes: (240.6680) Surface plasmons; (050.2230) Fabry-Perot; (140.4780) Optical resonators; (230.7370) Waveguides.

References and links

1. E. Kretschmann and H. Raether, "Radiative decay of non radiative surface plasmons excited by light," *Zeitschrift Fur Naturforschung Part A-Astrophysik Physik Und Physikalische Chemie A* **23**, 2135–2136 (1968).
2. U. Kreibig and L. Genzel, "Optical absorption of small metallic particles," *Surf. Sci.* **156**, 678–700 (1985).
3. J. N. Anker, W. P. Hall, O. Lyandres, N. C. Shah, J. Zhao, and R. P. Van Duyne, "Biosensing with plasmonic nanosensors," *Nat. Mater.* **7**(6), 442–453 (2008).
4. H. A. Atwater and A. Polman, "Plasmonics for improved photovoltaic devices," *Nat. Mater.* **9**(3), 205–213 (2010).
5. E. Ozbay, "Plasmonics: Merging photonics and electronics at nanoscale dimensions," *Science* **311**(5758), 189–193 (2006).
6. D. Schurig, J. J. Mock, B. J. Justice, S. A. Cummer, J. B. Pendry, A. F. Starr, and D. R. Smith, "Metamaterial electromagnetic cloak at microwave frequencies," *Science* **314**(5801), 977–980 (2006).
7. Y. G. Sun, B. Gates, B. Mayers, and Y. N. Xia, "Crystalline silver nanowires by soft solution processing," *Nano Lett.* **2**(2), 165–168 (2002).
8. H. Ditlbacher, A. Hohenau, D. Wagner, U. Kreibig, M. Rogers, F. Hofer, F. R. Aussenegg, and J. R. Krenn, "Silver nanowires as surface plasmon resonators," *Phys. Rev. Lett.* **95**(25), 257403 (2005).
9. J. Takahara, S. Yamagishi, H. Taki, A. Morimoto, and T. Kobayashi, "Guiding of a one-dimensional optical beam with nanometer diameter," *Opt. Lett.* **22**(7), 475–477 (1997).
10. R. M. Dickson and L. A. Lyon, "Unidirectional plasmon propagation in metallic nanowires," *J. Phys. Chem. B* **104**(26), 6095–6098 (2000).
11. R. Gordon, "Reflection of cylindrical surface waves," *Opt. Express* **17**(21), 18621–18629 (2009).
12. R. Zia, J. A. Schuller, and M. L. Brongersma, "Near-field characterization of guided polariton propagation and cutoff in surface plasmon waveguides," *Phys. Rev. B* **74**(16), 165415 (2006).
13. J. C. Weeber, A. Dereux, C. Girard, J. R. Krenn, and J. P. Gouyonnet, "Plasmon polaritons of metallic nanowires for controlling submicron propagation of light," *Phys. Rev. B* **60**(12), 9061–9068 (1999).
14. J. R. Krenn, B. Lamprecht, H. Ditlbacher, G. Schider, M. Salerno, A. Leitner, and F. R. Aussenegg, "Non diffraction-limited light transport by gold nanowires," *Europhys. Lett.* **60**(5), 663–669 (2002).
15. L. Novotny, "Effective wavelength scaling for optical antennas," *Phys. Rev. Lett.* **98**(26), 266802 (2007).
16. A. W. Sanders, D. A. Routenberg, B. J. Wiley, Y. N. Xia, E. R. Dufresne, and M. A. Reed, "Observation of plasmon propagation, redirection, and fan-out in silver nanowires," *Nano Lett.* **6**(8), 1822–1826 (2006).
17. R. X. Yan, P. Pausauskie, J. X. Huang, and P. D. Yang, "Direct photonic-plasmonic coupling and routing in single nanowires," *Proc. Natl. Acad. Sci. U.S.A.* **106**(50), 21045–21050 (2009).
18. X. W. Chen, V. Sandoghdar, and M. Agio, "Highly efficient interfacing of guided plasmons and photons in nanowires," *Nano Lett.* **9**(11), 3756–3761 (2009).

19. X. Guo, M. Qiu, J. M. Bao, B. J. Wiley, Q. Yang, X. N. Zhang, Y. G. Ma, H. K. Yu, and L. M. Tong, "Direct coupling of plasmonic and photonic nanowires for hybrid nanophotonic components and circuits," *Nano Lett.* **9**(12), 4515–4519 (2009).
20. F. Hao and P. Nordlander, "Plasmonic coupling between a metallic nanosphere and a thin metallic wire," *Appl. Phys. Lett.* **89**(10), 103101 (2006).
21. M. W. Knight, N. K. Grady, R. Bardhan, F. Hao, P. Nordlander, and N. J. Halas, "Nanoparticle-mediated coupling of light into a nanowire," *Nano Lett.* **7**(8), 2346–2350 (2007).
22. Y. R. Fang, Z. P. Li, Y. Z. Huang, S. P. Zhang, P. Nordlander, N. J. Halas, and H. X. Xu, "Branched silver nanowires as controllable plasmon routers," *Nano Lett.* **10**(5), 1950–1954 (2010).
23. H. Wei, Z. Li, X. Tian, Z. Wang, F. Cong, N. Liu, S. Zhang, P. Nordlander, N. J. Halas, and H. Xu, "Quantum dot-based local field imaging reveals plasmon-based interferometric logic in silver nanowire networks," *Nano Lett.* **11**(2), 471–475 (2011).
24. A. V. Akimov, A. Mukherjee, C. L. Yu, D. E. Chang, A. S. Zibrov, P. R. Hemmer, H. Park, and M. D. Lukin, "Generation of single optical plasmons in metallic nanowires coupled to quantum dots," *Nature* **450**(7168), 402–406 (2007).
25. D. E. Chang, A. S. Sørensen, P. R. Hemmer, and M. D. Lukin, "Quantum optics with surface plasmons," *Phys. Rev. Lett.* **97**(5), 053002 (2006).
26. T. Shegai, Y. Z. Huang, H. X. Xu, and M. Käll, "Coloring fluorescence emission with silver nanowires," *Appl. Phys. Lett.* **96**(10), 103114 (2010).
27. A. L. Falk, F. H. L. Koppens, C. L. Yu, K. Kang, N. de Leon Snapp, A. V. Akimov, M.-H. Jo, M. D. Lukin, and H. Park, "Near-field electrical detection of optical plasmons and single-plasmon sources," *Nat. Phys.* **5**(7), 475–479 (2009).
28. H. Wei, D. Ratchford, X. E. Li, H. X. Xu, and C. K. Shih, "Propagating surface plasmon induced photon emission from quantum dots," *Nano Lett.* **9**(12), 4168–4171 (2009).
29. J. Dorfmueller, R. Vogelgesang, R. T. Weitz, C. Rockstuhl, C. Etrich, T. Pertsch, F. Lederer, and K. Kern, "Fabry-Pérot resonances in one-dimensional plasmonic nanostructures," *Nano Lett.* **9**(6), 2372–2377 (2009).
30. J. Dorfmueller, R. Vogelgesang, W. Khunsin, C. Rockstuhl, C. Etrich, and K. Kern, "Plasmonic nanowire antennas: experiment, simulation, and theory," *Nano Lett.* **10**(9), 3596–3603 (2010).
31. E. R. Encina and E. A. Coronado, "Plasmonic nanoantennas: Angular scattering properties of multipole resonances in noble metal nanorods," *J. Phys. Chem. C* **112**(26), 9586–9594 (2008).
32. T. Shegai, V. D. Miljković, K. Bao, H. Xu, P. Nordlander, P. Johansson, and M. Käll, "Unidirectional broadband light emission from supported plasmonic nanowires," *Nano Lett.* **11**(2), 706–711 (2011).
33. Z. P. Li, F. Hao, Y. Z. Huang, Y. R. Fang, P. Nordlander, and H. X. Xu, "Directional light emission from propagating surface plasmons of silver nanowires," *Nano Lett.* **9**(12), 4383–4386 (2009).
34. Z. P. Li, K. Bao, Y. R. Fang, Y. Z. Huang, P. Nordlander, and H. X. Xu, "Correlation between incident and emission polarization in nanowire surface plasmon waveguides," *Nano Lett.* **10**(5), 1831–1835 (2010).
35. L. M. Tong, V. D. Miljković, and M. Käll, "Alignment, rotation, and spinning of single plasmonic nanoparticles and nanowires using polarization dependent optical forces," *Nano Lett.* **10**(1), 268–273 (2010).
36. P. B. Johnson and R. W. Christy, "Optical constants of noble metals," *Phys. Rev. B* **6**(12), 4370–4379 (1972).
37. P. Johansson, "Electromagnetic Green's function for layered systems: Applications to nanohole interactions in thin metal films," *Phys. Rev. B* **83**(19), 195408 (2011).
38. J. A. Stratton, *Electromagnetic Theory* (McGraw-Hill: New York, 1941).
39. P. Hanarp, M. Käll, and D. Sutherland, "Optical properties of short range ordered arrays of nanometer gold disks prepared by colloidal lithography," *J. Phys. Chem. B* **107**(24), 5768–5772 (2003).
40. F. Neubrech, T. Kolb, R. Lovrincic, G. Fehsold, A. Pucci, J. Aizpurua, T. Cornelius, M. Toimil-Molaes, R. Neumann, and S. Karim, "Resonances of individual metal nanowires in the infrared," *Appl. Phys. Lett.* **89**(25), 253104 (2006).
41. F. Neubrech, A. Pucci, T. W. Cornelius, S. Karim, A. García-Etxarri, and J. Aizpurua, "Resonant plasmonic and vibrational coupling in a tailored nanoantenna for infrared detection," *Phys. Rev. Lett.* **101**(15), 157403 (2008).
42. T. H. Taminiau, F. D. Stefani, and N. F. van Hulst, "Optical nanorod antennas modeled as cavities for dipolar emitters: evolution of sub- and super-radiant modes," *Nano Lett.* **11**(3), 1020–1024 (2011).

1. Introduction

Surface plasmons in metal nanostructures [1, 2] have attracted enormous recent interest because of a wide range of potential applications in areas such as biochemical sensing [3], photovoltaics [4], nanophotonics [5] and metamaterials [6]. However, much of this development would most likely not have occurred without the continuous development of sophisticated methods and software for electrodynamics simulations of nanooptical phenomena. In this paper, we present a method for calculating the differential scattering cross section of supported nanostructures using a combination of the Green's function method and a commercial finite element method (FEM) (Comsol multiphysics 3.5a). We believe that the methodology fills an important gap among the large number of existing computational techniques in that it makes it possible to simulate comparatively large metal structures that are optically close to an interface. Indeed, this is a situation that is encountered in practice in a

very large number of experimental plasmonics studies. Here we use the method to study the near-field and far-field properties of supported silver nanowires, but the method can in principle be applied to any nanostructure shape and material.

Progress in colloidal synthesis over the last two decades has allowed for the fabrication of a large diversity of metal nanostructures with high crystalline quality, in particular various types of nanowires [7, 8]. Metal nanowires are interesting from a photonics point-of-view because they can support surface plasmon polaritons (SPPs) that are propagating along one direction while being localized in the other two [8–16], a phenomenon that could be interesting for a number of applications. Recent reports pointing in this direction include investigations of coupling between plasmonic and photonic nanowires [17–19] and between nanoparticles and wires [20, 21], demonstrations of plasmon routing [22] and interferometric logics [23] and studies of how single photon emitters, such as quantum dots and fluorophores, couple to nanowires [24–28]. More fundamental studies on plasmonic nanowires include research on near field [29] and far field [30, 31] properties, emission directionality [32–34] and optical rotation [35].

Most of the experimental studies mentioned above deal with nanowires supported by an optically mismatched interface, and this is therefore the focus of the present study. We are particularly interested in understanding how plasmonic nanowires behave as Fabry Perot (FP) resonators and in characterizing the near-field and far-field properties of such systems. We also calculate the plasmon dispersion relations for supported nanowires of different diameters and compare the results with analytical models valid for homogeneous environments. Some of the calculations are compared with experimental results and a good agreement is found.

2. Methods

Our calculations combine the use of a commercial FEM package with the Green's function method and are carried out in two steps. First the total fields inside the scatterer are calculated using the finite element method and afterwards, as a second step, the far field distribution of the fields is calculated using the Green's functions for the two-layer background and the field inside the scatterer found in the first step as input.

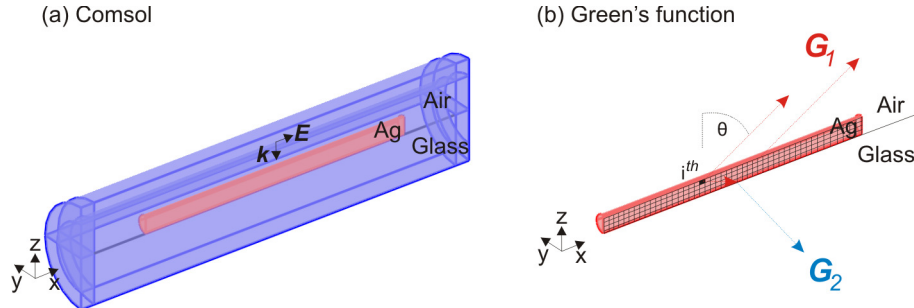


Fig. 1. Schematic of the calculation methods. (a) Comsol calculation domain for the calculations of the fields inside and in near surrounding of the nanowire. (b) Calculations of the differential scattering cross sections using the Green's function method and meshing of the nanowire.

For the FEM calculation, we use the RF module in the scattering formulation to find the electric field distribution inside, and in the near proximity of, a single silver nanowire, i.e. a cylinder with the radius R (we consider the cases $R = 40$ nm, $R = 80$ nm, and $R = 160$ nm in this work) and length $L = 5$ μ m. Figure 1(a) shows the Comsol simulation domain, with the interface between air and glass at $z = 0$ and the surroundings of the wire have refractive index $n_1 = 1$ for $z > 0$, and $n_2 = 1.5$ for $z < 0$. The wire has a refractive index of silver taken from Johnson and Christy [36]. In the FEM calculation the surroundings of the nanowire are delimited by two finite cylinders, the smaller with radius 600 nm and length 7 μ m and the bigger with radius 900 nm and the length 8 μ m. The part of space in between these cylinders

(blue color in the Fig. 1(a)) are perfectly matched layers (PML's), which absorb all the scattered light with minimal reflections. We apply scattering boundary conditions at the surface of the larger cylinder, i.e. that interface is transparent to the scattered light, and perfect magnetic conductor boundary conditions at $y = 0$ because the magnetic field is only directed along the y axis, which allows us to use the symmetry and simulate only half the wire.

The plane wave driving the system is incident along the z axis from the air side and is, using the Fresnel formulas, $\vec{E} = (E_x, 0, 0)$ where E_x is

$$E_x = \begin{cases} E_0 e^{-ik_0 n_1 z} (1 - r e^{2ik_0 n_1 z}) & , z > 0 \\ E_0 t e^{-ik_0 n_2 z} & , z \leq 0 \end{cases}, \quad (1)$$

and E_0 is the magnitude of the field, k_0 is the wave number in vacuum, $r = \frac{n_1 - n_2}{n_1 + n_2}$ is the

reflection magnitude and $t = \frac{2n_1}{n_1 + n_2}$ is the transmission magnitude for normal incidence at the

air-glass interface. Here we use a time dependence $e^{-i\omega t}$, whereas Comsol uses the electrical engineering convention with a time dependence $e^{i\omega t}$, which means that the arguments of the exponential functions in Eq. (1) should have an opposite sign when the equation is implemented in that software.

After solving the model, the field distribution inside and in the proximity of the nanowire is known. In order to find differential scattering cross sections of the nanowire, we then use the Green's function method [37]. Here, we derive an analytical formula of the asymptotic Green's function for the case of a single interface, which is easy to implement. It provides a generalization to the case of a layered background of the Stratton-Chu formula [38] that is built into the Comsol software.

The differential scattering cross section can be calculated as,

$$\frac{d\sigma}{d\Omega}(\theta, \varphi) = \frac{r^2 S_{far}}{S_{in}}, \quad (2)$$

where S_{far} is the radial component of the Poynting vector at a large distance r , S_{in} is the Poynting vector magnitude of the incident field, and the scattering direction is defined by the spherical coordinate angles θ and φ . In our case the field is incident from the air side, while the scattered fields propagate in both air (labeled with index 1) and glass (labeled with index 2), so that the corresponding Poynting vector magnitudes can be calculated as,

$$S_{far}^{1(2)} = \frac{1}{2} c \varepsilon_0 \sqrt{\varepsilon_{1(2)}} |\vec{E}(\vec{r})|^2, \quad (3)$$

$$S_{in}^1 = \frac{1}{2} c \varepsilon_0 \sqrt{\varepsilon_1} |\vec{E}^0|^2, \quad (4)$$

where $\vec{E}(\vec{r})$ is the scattered field from the nanowire (in a direction defined with angles θ and φ) and \vec{E}^0 is the magnitude of the incident field.

The scattered electric fields from a nanostructure can be calculated by discretizing the electric fields on a mesh with equally sized cubic elements (see Fig. 1(b)), summing contributions from each mesh element [37],

$$\vec{E}(\vec{r}) = \sum_{i=1}^N \vec{G}(\vec{r}, \vec{r}_i') k_0^2 \Delta \varepsilon_i \vec{E}_i V_i, \quad (5)$$

where k_0 is the wave vector in vacuum, $\Delta \varepsilon_i = \varepsilon_i - \varepsilon_1$, ε_i is the relative dielectric permittivity of the scatterer (in our case ε_i is dielectric permittivity of silver), ε_1 is dielectric permittivity of the surrounding medium (in our case the wire is in air, thus $\varepsilon_1 = 1$), $V_i = a_M^3$ is the volume of the cubic mesh element with size a_M (we use $a_M = 5$ nm), $\vec{E}_i = (E_{x,i}, E_{y,i}, E_{z,i})$ is the total field at the position of i^{th} mesh element (in our case, those fields were calculated using FEM), and $\vec{G}(\vec{r}, \vec{r}_i')$ is the Green's function, which describes field propagation in a direction specified by the angles θ and φ .

In the following, we present expressions for the asymptotic Green's functions at a single interface positioned at $z = 0$ as shown in Fig. 1. The asymptotic Green's function G_1 on the air side (i.e. for $z > 0$ or $0 < \theta < \pi/2$ in spherical coordinates) and G_2 on the glass side (i.e. for $z < 0$, or $\pi/2 < \theta < \pi$) can be calculated as follows,

$$\vec{G}_1(\vec{r}, \vec{r}_i') = \frac{e^{ik_1 r}}{4\pi r} e^{-i\vec{k}_{\parallel} \cdot \vec{r}_i'} e^{-ik_{z1} z} \left[\hat{p}_1^+ \otimes \hat{p}_1^+ + \hat{s} \otimes \hat{s} + e^{2ik_{z1} z} (r_p \hat{p}_1^+ \otimes \hat{p}_1^- + r_s \hat{s} \otimes \hat{s}) \right], \quad (6)$$

$$\vec{G}_2(\vec{r}, \vec{r}_i') = \frac{e^{ik_2 r}}{4\pi r} e^{-i\vec{k}_{\parallel} \cdot \vec{r}_i'} \frac{k_{z2}}{k_{z1}} e^{ik_{z1} z} \left[t_p \hat{p}_2^- \otimes \hat{p}_1^- + t_s \hat{s} \otimes \hat{s} \right], \quad (7)$$

where $k_{1(2)} = \sqrt{\varepsilon_{1(2)}} k_0$ is the magnitude of the wave vector in air (glass), $\vec{r}_i' = (x_i, y_i, z_i)$ are coordinates of the mesh elements, \otimes is dyadic product that makes the Green's function a 3×3 matrix, and the in-plane wave vector is $\vec{k}_{\parallel} = k_{1(2)} (\sin \theta \cos \varphi, \sin \theta \sin \varphi, 0)$ when the field point is in air (glass). The z component of the wave vector in air (glass) is $k_{z1(2)} = \sqrt{k_{1(2)}^2 - k_{\parallel}^2}$, while the unit polarization vectors for s and p polarizations are given by

$$\hat{s} = (-\sin \varphi, \cos \varphi, 0) \quad (8)$$

$$\hat{p}_1^{\pm} = \left(\pm \frac{k_{z1}}{k_1} \cos \varphi, \pm \frac{k_{z1}}{k_1} \sin \varphi, -\frac{k_{\parallel}}{k_1} \right), \quad (9)$$

$$\hat{p}_2^- = \left(-\frac{k_{z2}}{k_2} \cos \varphi, -\frac{k_{z2}}{k_2} \sin \varphi, -\frac{k_{\parallel}}{k_2} \right). \quad (10)$$

The reflection and transmission amplitudes for s and p polarizations can be calculated as,

$$r_s = \frac{k_{z1} - k_{z2}}{k_{z1} + k_{z2}}, \quad t_s = 1 + r_s, \quad (11)$$

$$r_p = \frac{\varepsilon_2 k_{z1} - \varepsilon_1 k_{z2}}{\varepsilon_2 k_{z1} + \varepsilon_1 k_{z2}}, \quad t_p = \frac{k_2 k_{z1}}{k_1 k_{z2}} (1 - r_s). \quad (12)$$

From a physical point of view the Green's function $\vec{G}_1(\vec{r}, \vec{r}_i')$, from Eq. (6), describes the fields emitted from a mesh element at the position (x_i, y_i, z_i) to the far field on the air side, while $\vec{G}_2(\vec{r}, \vec{r}_i')$ in Eq. (7) describes fields transmitted into the glass side. In Eq. (6) the first two terms inside the brackets describe p and s polarized waves that are propagating into the

far field directly and the last two terms describe waves propagating in the same direction after having been reflected off the air-glass interface, while in Eq. (7) the Green's function $\tilde{G}_2(\vec{r}, \vec{r}_i)$ only involves waves that are transmitted through the air-glass interface.

3. Results and discussion

Figure 2 shows total scattering spectra for nanowires calculated in the three different environments air, glass and air-glass, respectively (for the air-glass case, spectra represent the total scattering to the glass side). The scattering from thin nanowires ($R = 40$ nm) displays a series of pronounced resonance peaks and, as we will see, the nanowire acts like a Fabry-Perot cavity for plasmons. Upon an increase of the wire thickness (green and blue curves), regardless of the environment, the resonances are weakened and almost completely vanish for $R = 160$ nm (blue dash-dotted lines).

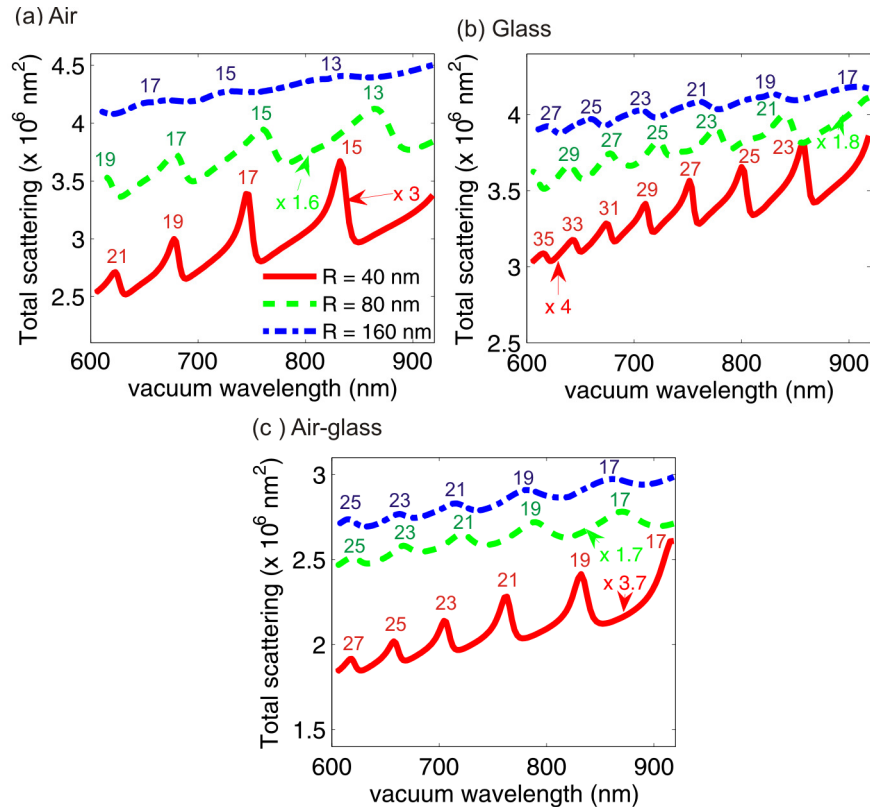


Fig. 2. (a-c) Total scattering spectra for thin ($R = 40$ nm), intermediate ($R = 80$ nm) and thick ($R = 160$ nm) nanowires calculated for three different surrounding media: (a) Wires surrounded by air; (b) Wires surrounded by glass; (c) Wires supported at an air-glass interface (the total spectra are calculated by integration of scattering in glass only). The corresponding mode orders l are shown above the each resonance.

Experimental scattering spectra for supported silver wires of different dimensions are summarized in Fig. 3. Propagating plasmons were in this case excited by focusing a fiber-coupled white-light source onto one end of a wire, which results in excitation of plasmon resonances of both even and odd symmetry. The scattering from the output end was then collected by the same objective ($60 \times \text{NA} = 1.49$ oil immersion) and sent to a fiber-coupled spectrometer, more details can be found elsewhere [32]. Also here, in good agreement with the calculated results, the standing wave resonances become more and more damped with increasing wire diameter, in spite of the somewhat different scattering geometries.

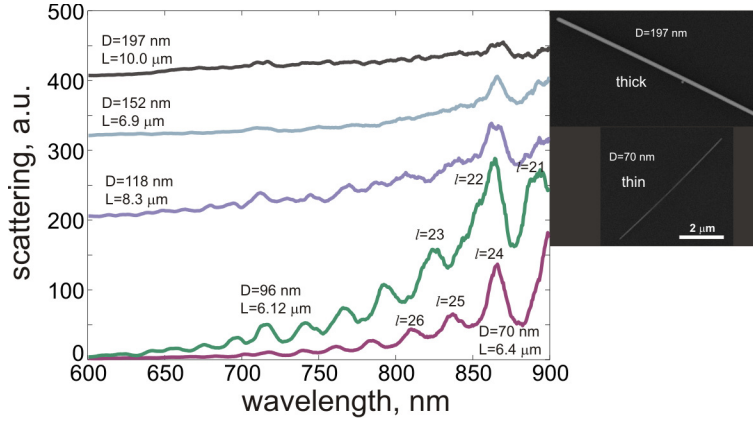


Fig. 3. Experimental scattering spectra for silver wires of different length and diameters supported by an air-glass interface. Similar to the calculations, thin wires show pronounced standing wave profiles while thick wires are poor resonators. Inset shows representative SEM images of $D = 70$ nm and $D = 197$ nm wires.

In order to understand the nanowire resonances it is useful to turn to the dispersion relation for plasmons propagating along an infinite cylinder. Figures 4(a)–4(c) show such dispersion relations for Ag cylinders with radius $R = 40$ nm, $R = 80$ nm and $R = 160$ nm, respectively. The solid lines represent the dispersion relation for TM₀ modes of a cylinder in a homogeneous environment [15] found from the solution of

$$\frac{\epsilon_m J_1(\kappa_1 R)}{\kappa_1 J_0(\kappa_1 R)} - \frac{\epsilon_d H_1^{(1)}(\kappa_2 R)}{\kappa_2 H_0^{(1)}(\kappa_2 R)} = 0, \quad (13)$$

where J_n and $H_n^{(1)}$ are cylindrical Bessel and Hankel functions, ϵ_m is the real part of the dielectric constant of silver, $\epsilon_d = n^2$ is the dielectric constant of the surrounding medium, and $\kappa_{1(2)} = k_0 \sqrt{\epsilon_{(d)} - (k_{\text{spp}} / k_0)^2}$. In our case the surrounding refractive index is $n = 1$ in air (red lines), $n = 1.5$ in glass (green lines), and $n = 1.25$ at the air-glass interface (blue lines). The crosses are calculated from the Fabry-Perot resonance condition [8, 29]

$$k_{\text{spp}} = \frac{l\pi - \phi_r}{L} \approx \frac{l\pi}{L}, \quad (14)$$

where l is the mode order found from the near-field patterns (ϕ_r is the phase shift upon reflection at the wire ends which here can be neglected because $l \gg 1$).

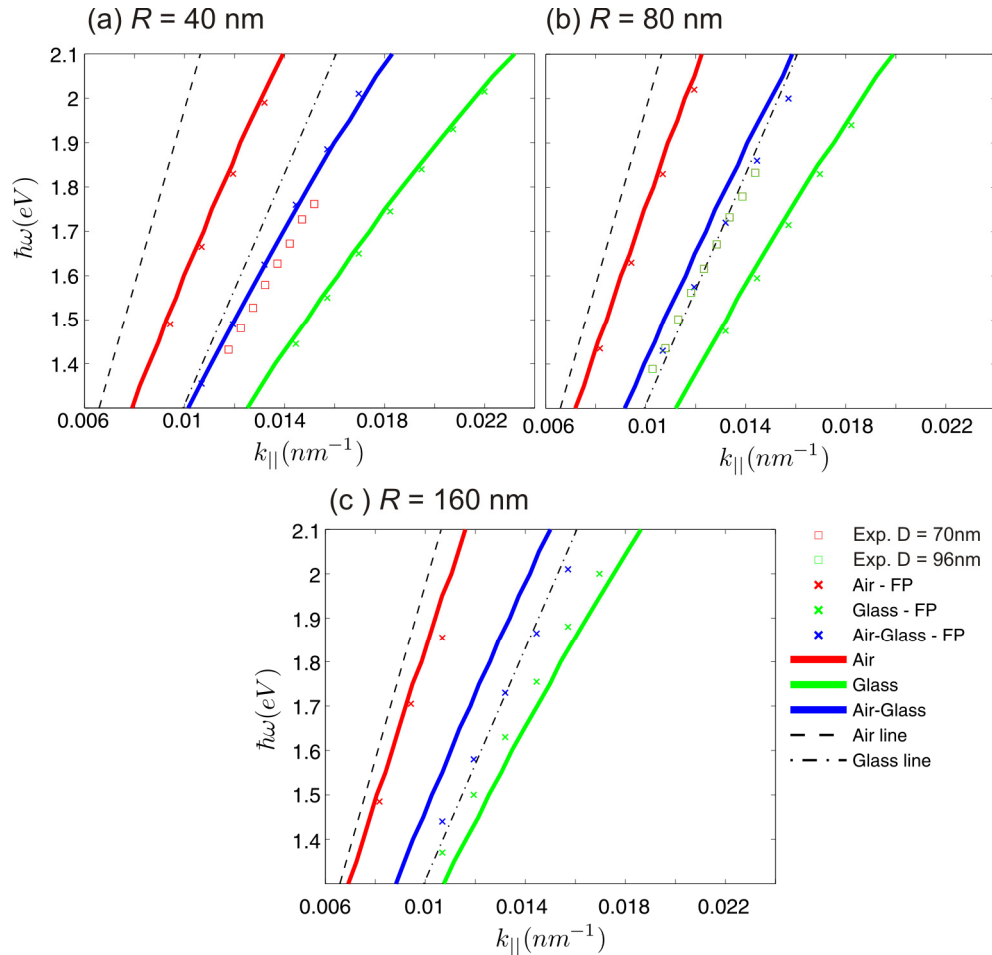


Fig. 4. (a-c) Dispersion relations calculated by extracting plasmon wavelengths from Fabry Perot model (crosses), analytical solution of infinite metal cylinder (solid lines), and from the experimental spectra (squares) for thin (a), intermediate (b), and thick (c) nanowires, respectively. The dispersions are calculated for wires in air (red), glass (green), and at an air-glass interface (blue). In addition, the light line in air (black dashed line) and the light line in glass (black dash-dotted line) are shown.

For thin wires (Fig. 4(a)), the dispersion relations extracted from the near field agrees very well with the analytic results derived from Eq. (13). As expected, the dispersion curve for a plasmon running along a wire in air (red lines) falls below the air light line (black dashed line), while for a wire in glass (green lines) it falls below the glass light line (black dashed-dotted line). Importantly, the case of the supported nanowire is very well approximated by a plasmon propagating along a wire immersed in a medium with refractive index $n = 1.25$, i.e. the average of the air and glass refractive indices. This result corroborates the refractive index averaging approximation used in many previous simulations of thin supported plasmonic nanoantennas, such as those in references [39–41]

For the thicker nanowires (Figs. 4(b), 4(c)), the plasmon dispersions on wires in the homogeneous media fall closer to the air and glass light lines, respectively. Effectively, we have a higher plasmon energy for thicker wires as a result of stronger restoring forces. However, the dispersion relation for the supported nanowires no longer follow the analytical solution calculated with an average refractive index, $n = 1.25$. As we will see, not only charge oscillations along the wire play a role as the wire gets thicker. Instead, other degrees of freedom gain importance and the fields at the top and the bottom of the wire becomes more

and more decoupled. To roughly distinguish between thin and thick wires in this context, we compare the wire circumference (which is about 250 nm, 500 nm, and 1000 nm, respectively, for the wire radii we consider here) with the plasmon wavelength ($2\pi/k_{||}$), which here lies in the interval 400-600 nm.

Squares in Figs. 4(a), 4(b) show the dispersion relations for the two thinnest wires calculated from the experimental standing wave profiles spectra in Fig. 3 using Eq. (14), where we have to assume the resonance order for those wires (as shown in the Fig. 3). The agreement between experimental and calculated dispersions is very good for thin wires.

Turning to the calculated near-field patterns, Figs. 5(a)–5(c) show the intensity of the total fields calculated for thin nanowires ($R = 40$ nm) in air, glass and at the air-glass interface at wavelengths 745 nm, 751 nm and 763 nm, respectively. These field patterns show in a very clear way the existence of the Fabry-Perot resonances discussed above, and it is possible to find the mode order l of each of the peaks seen in the spectra by counting the number of nodes in the near field intensity (the mode order is shown above each resonance peak in Fig. 2). At approximately equal photon energies, the nanowires embedded in glass yields the highest mode order $l = 27$, the nanowires in air yields the lowest mode order, $l = 17$, while the order of the resonance for supported nanowire is $l = 21$. In terms of SPP wavelengths we thus have $\lambda_{spp}^{air} > \lambda_{spp}^{air-glass} > \lambda_{spp}^{glass}$. We see that the plasmon fields at the top (air) and bottom (glass) edges of the nanowire are in phase with each other. This means that in the case of a thin supported nanowire it is mainly the cylindrically symmetric plasmons (with an azimuthal quantum number $m = 0$) that are excited. Comparing the different dielectric environments in Fig. 5, the nanowires embedded in air gives the largest field enhancement. The fields penetrate more easily into the metal for a denser surrounding medium leading to a decrease in the field enhancement for the wires embedded in glass. For supported nanowires the strongest fields appear near the glass interface due to the well known image dipole interaction.

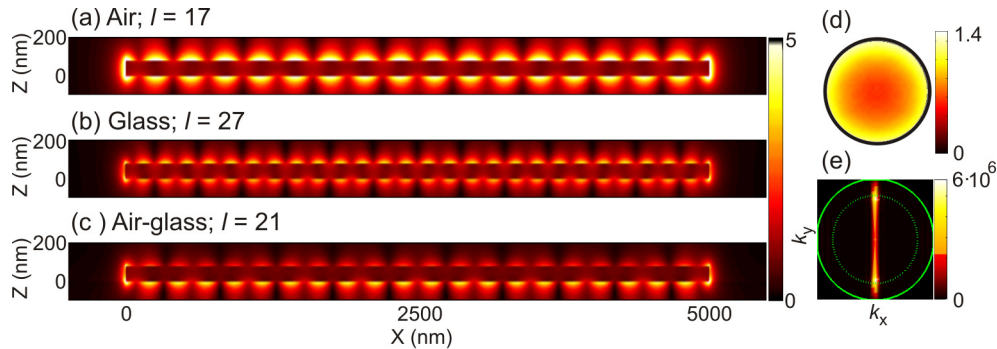


Fig. 5. Electric field intensity along xz plane for thin nanowires in air (a), glass (b), and at an air-glass interface (c). The fields are calculated for corresponding resonance peaks at vacuum wavelength ~ 750 nm (see Fig. 2). (d) Corresponding electric field distribution inside the supported nanowire at $x = 2500$ nm. (e) Fourier image of radiation in glass substrate for thin nanowire calculated at 763 nm.

Figure 5(e) shows calculated results for the far field scattering to the glass side on the Fourier plane for the supported nanowire at free-space wavelength $\lambda = 763$ nm, where $k_x = k_{glass} \sin(\theta) \cos(\varphi)$, $k_y = k_{glass} \sin(\theta) \sin(\varphi)$ and $k_{glass} = 2\pi n / \lambda$ is the wave number in glass. The inner green dashed line represents the border ($k_{||} = k_{air}$) between propagating and evanescent waves in air, while the green solid line represents the same border ($k_{||} = k_{glass}$) for waves in glass. The light that is scattered inside the dashed circle is often termed “allowed” light, while the light between the dashed and the solid circle is termed “forbidden”. The scattering is concentrated to in-plane directions that are perpendicular to the nanowire and peaks at angles near the critical angle for the air-glass interface, i.e. 41.8 degrees. This radiation pattern is in agreement with previously published results on emission from nanowires in homogeneous media involving higher order resonance modes [30, 31, 42]. As is known from these

publications, the higher order odd resonances in the nanowires radiate mostly perpendicular to the wire orientation, with some weaker side lobes. The currents in the nanowire largely give a radiation pattern similar to that occurring from a chain of dipoles oscillating in phase. In case the incident field hits the wire at an angle, there will be phase differences between the currents along the wire that moves the scattering maximum to a finite k_x given by the momentum of the incident photons along the wire. The width of the central lobe (or stripe) along the k_x direction is determined by the length of the wire, since the first minimum, according to multi-slit diffraction theory occurs when $k_x \approx 2\pi/L$.

Figure 6(a), 6(b) show near field intensities of the total field around supported nanowires with radius $R = 80$ nm and $R = 160$ nm, respectively. These wires can be characterized as thick (for the photon energy in question) since, as pointed out above, now the wire circumference reaches values, approximately 500 nm and 1000 nm, respectively, that are comparable to, or larger than the plasmon wavelength. Compared to the thin nanowire (Fig. 5(c)), the near field intensity is much weaker here. The field patterns along the top and bottom edges of the wire differ quite a lot in this case, indicating a decoupling between the plasmons at opposite edges of the wire. Consequently, more plasmon modes are involved in forming the field in and around a thicker nanowire than was the case for $R = 40$ nm. The plasmons appearing here are hybridized modes, primarily between $m = 0$ and $m = 1$ modes of a wire in a homogeneous environment.

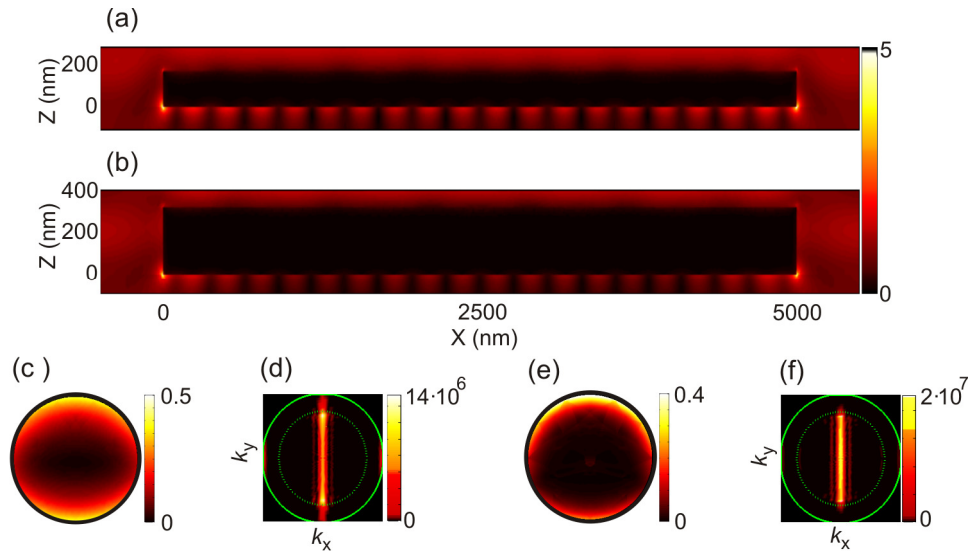


Fig. 6. Electric field intensity along xz plane for intermediate (a) and thick (b) nanowires supported at an air-glass interface. The corresponding vacuum wavelengths are 787 nm and 785 nm, respectively. (c, e) Corresponding electric field distribution inside intermediate and thick nanowires at $x = 2500$ nm. (d, f) Corresponding Fourier images of the radiation scattered into the glass substrate for the intermediate and thick nanowires shown in (a,b).

Figures 6(d), 6(f) show Fourier images on the glass side for supported nanowires with $R = 80$ nm and $R = 160$ nm, respectively. Again, we have a sharp maximum at $k_x = 0$ flanked by rather weak but still visible side lobes. Compared with Fig. 5, we see that with increasing nanowire thickness, more light is scattered inside the dashed circle, i.e. in the “allowed” region. In other words, propagating scattered light dominates over evanescent light for thicker wires. This can be understood from the fact that more and more of the scattering volume is removed from the immediate vicinity of the air-glass interface as the wire radius is increased. Still, if the parts of the wire right next to the surface gave the dominating contributions to the scattering we would not see this trend. While Figs. 6(a) and 6(b) appear to indicate a concentration of the fields to the glass side of the wire, this is the situation *outside* the wire. However, as can be seen from Eq. (5), what matters in determining the scattered fields is how

the electric field *inside* the wire behave. For the thicker wires, one finds the strongest fields along the top rim of the wire and right near the glass surface as shown in Fig. 6(c), (e).

4. Summary and conclusion

In conclusion, we have investigated far field and near field properties of silver nanowires supported by a glass substrate using a method which calculates differential scattering cross sections based on the total fields inside the wire obtained using a commercial finite element software (Comsol multiphysics 3.5a). For supported thin wires, which are much better resonators than thick wires, we find that the fields on the air and glass sides are in phase with each other. The spectral properties of such wires can be then be understood from the dispersion of cylinder plasmons in a homogeneous environment with a refractive index intermediate between air and glass. However, the dispersion starts to deviate from the average refractive index approximation as the wire diameter increases beyond the plasmon wavelength, because the fields along the different edges of the wire then decouple from each other. Looking at the fields inside the wires, which ultimately are the sources for the scattered light, there are also clear differences between thin and thick wires. In particular, the fields in the thicker wires are mainly concentrated to the top rim of the wire while they are more evenly distributed in a thin wire. Finally, we compared the simulation results with experimentally measured spectra and found an excellent agreement. Further issues that could be addressed using our method include how the shape of the wire-tip influences the optical properties, the question on optical coupling and plasmon propagation between two wires of different shape, length or diameter, and the role of crystal facets and wire imperfections.

Acknowledgment

This work was financially supported by the Swedish Research Council and the Göran Gustafsson Foundation.